Hindawi
International Journal of Aerospace Engineering
Volume 2022, Article ID 8091927, 16 pages
https://doi.org/10.1155/2022/8091927

*Research Article*

# Effects of the Air Inlet Angle on the Combustion and Ablation Environment of a Hybrid Powder-Solid Ramjet

**Jinjin Wang,[1] Yihao Wen ,[1] Bailin Zha,[1] Zhigao Xu,[1] and Tianhao Zhang[2]**

[1]*Rocket Force University of Engineering, Xi'an 710025, China*
[2]*Key Laboratory of Non-Destructive Testing of Ministry of Education, Nanchang Hangkong University, Nanchang, 330063 Jiangxi, China*

Correspondence should be addressed to Yihao Wen; hgdwenyihao@163.com

Received 23 September 2021; Revised 27 January 2022; Accepted 5 February 2022; Published 18 March 2022

Academic Editor: Jun-Wei Li



A hybrid powder-solid ramjet (HPSR) that combined the advantages of a solid rocket ramjet (SRJ) and a powder ramjet engine was investigated in this research. To improve the combustion efficiency and optimize the inner wall thermal protection of the afterburner, the effects of the air inlet angle on the combustion and wall ablation environment were studied. The standard $k$-$\varepsilon$ model, the eddy-dissipation model (EDM), and the boron particle ignition and combustion model were adopted to simulate the two-phase flow in the afterburners with different air inlet angles (45°, 60°, 75°, and 90°). The results showed that the global flow field and the distribution of the vortexes in the afterburner that had a significant influence on the ablation environment of the inner wall and the combustion efficiency were determined by the impact effect and the squeezing effect of the ram air on the primary fuel gas, which was affected by the air inlet angle. As the air inlet angle increased, the total combustion efficiency of the four cases first increased and then decreased, reaching 80.38%, 81.64%, 84.34%, and 83.26% for angles of 45°, 60°, 75°, and 90°, respectively. At the same time, the inner wall ablation became more severe because both the erosion effect of the condensed phase particles and the gas-flow scouring effect were enhanced, and a large temperature gradient was generated on the inner wall. The study results can provide a reference for designing the air inlet angle of an HPSR.

## 1. Introduction

Ducted rockets with important military significance have been developed for several decades [1–4]. To improve the comprehensive performance of ducted rockets, researchers usually apply a high-energy propellant with metallic particles or optimize the structure of a ramjet engine [5–9].

High-energy density fuel formulations containing polymer with embedded metal particles, including aluminum, magnesium, and boron, have been adopted in ducted rockets for decades [10–14]. Boron has a higher volume and calorific value than other metals, and its combustion products are in the gas phase in a high temperature environment, which will not cause thrust loss, so boron has been considered the most attractive fuel for ducted rockets. The combustion of boron particles in an afterburner is a well-explored subject [15–19]. Odawara et al. [15] researched the ignition delay time of boron particles in a combustion chamber and analyzed the ignition and combustion characteristics of gas generators containing boron. Natan and Gany [16] investigated the burning behavior of a single boron particle and found that there was a particle size and injection velocity range conducive to maintaining the combustion. Gany [17] studied the thermodynamic conditions associated with highly boron-loaded ramjet combustors and predicted the conditions for blocking reactions within a certain range of room pressures and temperatures. Liu et al. [18] developed a new experimental system to study the combustion of boron particles in a ducted rocket, and they provided some suggestions to optimize the structure of an afterburner to obtain a higher completion rate of boron combustion. Hashim et al. [19] used a low-cost screening instrument called an opposed flow burner (OFB) to investigate the effects of the size of boron particles on combustion by testing pure hydroxyl-terminated polybutadiene (HTPB) and HTPB loaded with boron nanoparticles

at various concentrations (5%–40% by wt.). In short, previous scholars [15–19] have performed comprehensive studies of boron particles and given detailed descriptions of the ignition and combustion process of boron particles in ramjets. Therefore, in the current work, HTPB propellant containing boron was adopted.

However, it is difficult to adjust the content of boron particles and the thrust of a solid rocket ramjet. Therefore, a new ramjet, called a hybrid powder-solid ramjet (HPSR), was investigated. The HPSR combined the advantages of a powder ramjet and the solid ramjet to adjust the powder flow rate and achieve the self-sustaining burn of metal particles easily [20]. In addition, many studies have focused on optimizing the structure of a ramjet to improve its comprehensive performance [20–26]. Zvuloni et al. [21] investigated the effects of the geometry and size on the combustion in a solid fuel ramjet (SFRJ) through experiments and found that the mean average regression rate decreased with the increasing gas port diameter. Vigot et al. [22] studied a ducted rocket with a double gas inlet with a theoretical analysis, demonstrating that the double gas inlet divided the inner flow field into two parts with a significant difference in the temperature and oxygen concentrations. Pein and Vinnemeier [23] carried out an experiment to study an SFRJ with a swirler and showed that the swirl flow strongly increased the combustion efficiency, until a maximum was reached at about 20%. Furthermore, Liu et al. [24] conducted a study on a turbocharged solid ramjet with an afterburner that combined the head region inlet and the lateral inlet and found that the radial and tangential momentum exchange of the air-fuel streams was enhanced by driving the compressed air to deflect inward. Musa et al. [25] performed an experimental investigation on an SFRJ with a new design swirler. It was revealed that increasing the swirl number and the combustor length increased the thrust and the characteristic velocity but decreased the air-fuel ratio and the specific impulse, while the increase of the port diameter was diametrically opposite. Xu et al. [20] investigated the effect of the tangential swirl air inlet angle in an HPSR and found that the ignition distance was decreased, and the combustion efficiency was increased with the increase of the angle. Li et al. [26] investigated an SFRJ that included a primary gas generator with a swirler and found that increasing the swirl number could enhance the combustion heat release rate, regression rate, and combustor average temperature.

In summary, although many studies on the structural factors of an afterburner have been carried out, few studies have focused on the effect of the air inlet angle [20–26]. Additionally, most studies have focused on combustion efficiency, while few have focused on the inner wall ablation of the combustion chamber. However, when an aircraft with a ramjet is performing a high-speed maneuverer, it has to withstand high overloads and a two-phase flow carrying a high concentration of condensed phase particles forms in the combustion chamber, worsening the working environment of the thermal insulation layer. In severe cases, this leads to the failure of the thermal insulation protection and even causes the ramjet to burn through and explode [27, 28]. Therefore, to ensure the reliable thermal protection of a ramjet, it is important to investigate the inner wall ablation environment of the afterburner.

In this work, an HPSR afterburner with symmetrical air inlets was established, and the effects of various air inlet angles (45°, 60°, 75°, and 90°) on the combustion efficiency and inner wall ablation environment were analyzed. The primary focus was on the following aspects: (i) the effects of the air inlet angle on the inner flow field of the afterburners, (ii) the effects of the air inlet angle on the combustion efficiency, and (iii) the effects of the air inlet angle on the inner wall ablation environment. Due to limited research on the effects of various air inlet angles on the combustion efficiency and the inner wall ablation environment, this paper can provide a reference to improve the comprehensive performance of an HPSR from the perspective of designing the air inlet angle.

## 2. Engine Model

Figure 1 shows the structure of the afterburner of the HPSR. The total length of the afterburner was 900 mm. The head length was 250 mm. The main body radius was 88 mm. The primary gas generator nozzle radius was 20 mm. The radius of the nozzle throat was 65 mm. The angle of the air inlet was denoted using $\theta$. To study the comprehensive effect of the air inlet angle on the afterburner, four cases were selected as case 1, case 2, case 3, and case 4, with inlet angles of 45°, 60°, 75°, and 90°, respectively.

To simplify the model, the following assumptions were made for the internal flow field of the afterburner.

(1) The gas jet in the afterburner had quasisteady flow, regardless of the heat exchange between the gas and the wall of the afterburner

(2) The gas in the afterburner was an ideal gas that obeyed the ideal gas state equation

## 3. Numerical Setup

*3.1. Two-Phase Flow Governing Equation.* According to the above assumptions, the Reynolds-Averaged Navier-Stokes equation was adopted as the gas-phase governing equation. The general forms of the continuum equation, the momentum equation, the energy equation, and the composition equation could be written as

$$\frac{\partial \mathbf{Q}}{\partial t} + \frac{\partial \mathbf{F}_x}{\partial x} + \frac{\partial \mathbf{F}_y}{\partial y} + \frac{\partial \mathbf{F}_z}{\partial z} = \frac{\partial \mathbf{G}_x}{\partial x} + \frac{\partial \mathbf{G}_y}{\partial y} + \frac{\partial \mathbf{G}_z}{\partial z} + \mathbf{H}, \quad (1)$$

where $t$ is time, $x$ is the $X$ direction, $y$ is the $Y$ direction, and $z$ is the $Z$ direction. $\mathbf{Q}$ is the conservative vector, $\mathbf{F}$ is the vector of convective flux, $\mathbf{G}$ is the vector of viscous flux, and $\mathbf{H}$ is the vector of source terms.

The particle phase governing equation employed the Lagrangian particle trajectory model [29, 30]. The force balance equation could be written as:

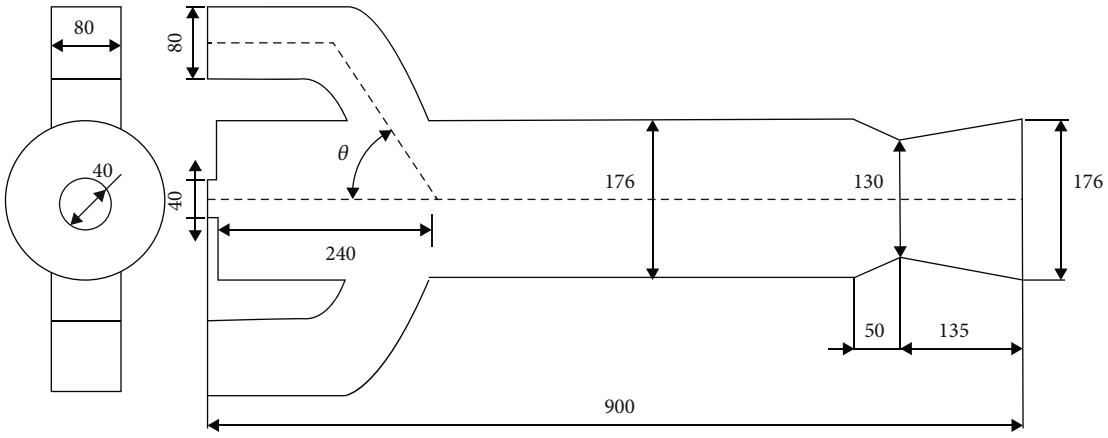


Figure 1: Structure of afterburners.

$$\frac{du_{\mathrm{p}}}{dt} = F_{\mathrm{D}}\left(u - u_{\mathrm{p}}\right) + g_x\left(\rho_{\mathrm{p}} - \rho\right). \tag{2}$$

The track equation of the particle in the $x$ direction could be written as:

$$\frac{dx}{dt} = u_{\mathrm{p}}, \tag{3}$$

where $u_{\mathrm{p}}$ is the instantaneous velocity of particles, $g_x$ is the component of gravitational acceleration in the $X$ direction, and $\rho_{\mathrm{p}}$ is the density of the particles. $u$ and $\rho$ are the velocity and the density of the fluid, respectively. $F_{\mathrm{D}}$ is the external force of the particles. $F_{\mathrm{D}}(u - u_{\mathrm{p}})$ is the drag force per unit mass.

To simulate the three-dimensional multiphase turbulent and reacting flow in the afterburner of the HPSR, the finite-volume method was adopted to discretize the RANS equations with the software program FLUENT. The theoretical formulation was solved using a numerical scheme based on the semi-implicit method for pressure linked equations (SIMPLE). The second order upwind scheme was utilized to compute the convective flux quantities. The standard $k$-$\varepsilon$ model with stable convergence, appropriate accuracy, and a small amount of calculation was used to address the turbulence in the afterburner [31, 32].

### 3.2. Combustion Model

*3.2.1. Gas-Phase Combustion Model.* The gas-phase combustion model employed the single-step reaction eddy-dissipation model (EDM) [33, 34], in which it was assumed that the combustion in the afterburner was a simple chemical reaction system with only two main reactions occurring, as follows:

$$\begin{cases} \mathrm{CO} + \mathrm{O_2} \longrightarrow 2\mathrm{CO_2}, \\ 2\mathrm{H_2} + \mathrm{O} \longrightarrow 2\mathrm{H_2O}. \end{cases} \tag{4}$$

*3.2.2. Boron Particle Ignition and Combustion Model.* The typical ignition and combustion models of boron particles include King's model [35–37] and Williams's model [38]. The former has a more definite physical meaning and is easy to use to establish a mathematical model, which was chosen as the boron particle ignition and combustion model in this work. The mathematical model could be written as the following formula:

$$\begin{cases} d_{\mathrm{p}} = d_{\mathrm{B}} + 2\delta, \\ \dfrac{dd_{\mathrm{B}}}{dt} = -\dfrac{2R_{\mathrm{B}}\mathrm{M_B}}{\pi d_{\mathrm{B}}^2 \rho_{\mathrm{B}}}, \\ \dfrac{d\delta}{dt} = -\dfrac{(R_{\mathrm{B}}/2 - R_{\mathrm{E}} - R_{\mathrm{H}})M_{\mathrm{B_2O_3}}}{\pi d_{\mathrm{B}}^2 \rho_{\mathrm{B_2O_3}}}, \\ \dfrac{dT_p}{dt} = \dfrac{\dot{Q}}{\left(d_{\mathrm{B}}^3\pi/6\right)c_{p,\mathrm{B}}\rho_{\mathrm{B}} + \pi d_{\mathrm{B}}^2 \delta c_{p,\mathrm{B_2O_3}}\rho_{\mathrm{B_2O_3}}} \left(T_{\mathrm{p}} \neq 2450\mathrm{K}\right), \\ \dfrac{dT_p}{dt} = \dfrac{\dot{Q}}{\left(d_{\mathrm{B}}^3\pi/6\right)\rho_{\mathrm{B}}\Delta H_M} \left(T_{\mathrm{p}} = 2450\mathrm{K}\right), \end{cases} \tag{5}$$

where $d_{\mathrm{p}}$ is the diameter of the boron particle, $T_{\mathrm{p}}$ is the temperature of the boron particle, $\dot{Q}$ is the energy change during ignition, $\delta$ is the oxide layer thickness of the boron particle, $R_{\mathrm{E}}$ is the evaporation rate of the boron oxide layer, $R_{\mathrm{H}}$ is the rate at which the boron oxide layer reacts with water vapor, $R_{\mathrm{B}}$ and $d_{\mathrm{B}}$ are the consumption rate and the diameter of boron in the oxide layer, respectively, $M_{\mathrm{B_2O_3}}$ and $\rho_{\mathrm{B_2O_3}}$ are the molar mass and the density of $B_2O_3$, and $C_{\mathrm{p,B}}$ and $C_{\mathrm{p,B_2O_3}}$ are the specific heat capacity at a constant pressure of B and $B_2O_3$, respectively.

The burning rate of the boron particles can be listed as follows:

$$\dot{m}_{\mathrm{p}} = k d_{\mathrm{p}}^2 \pi P_{\mathrm{O_2}}, \tag{6}$$

where $P_{\mathrm{O_2}}$ is the partial pressure of oxygen in the reaction environment.

Table 1: Boundary conditions.

| Boundary name | Boundary type | Mass flow rate (kg/s) | Total pressure (MPa) | Total temperature (K) | Species |
|---|---|---|---|---|---|
| Inlet | Mass flow inlet | 0.24 | 0.5 | 1800 | 47% CO, 41% $N_2$, 10% $H_2$, 1% $H_2O$, 1% $CO_2$ |
| The entrance of the air inlet | Mass flow inlet | 4 | 0.5 | 573 | 21% $O_2$, 78% $N_2$, 1% $CO_2$ |
| Outlet | Pressure outlet | 0.24 | 0.026 | 300 | — |
| Inner wall | No-slip wall | — | — | — | — |

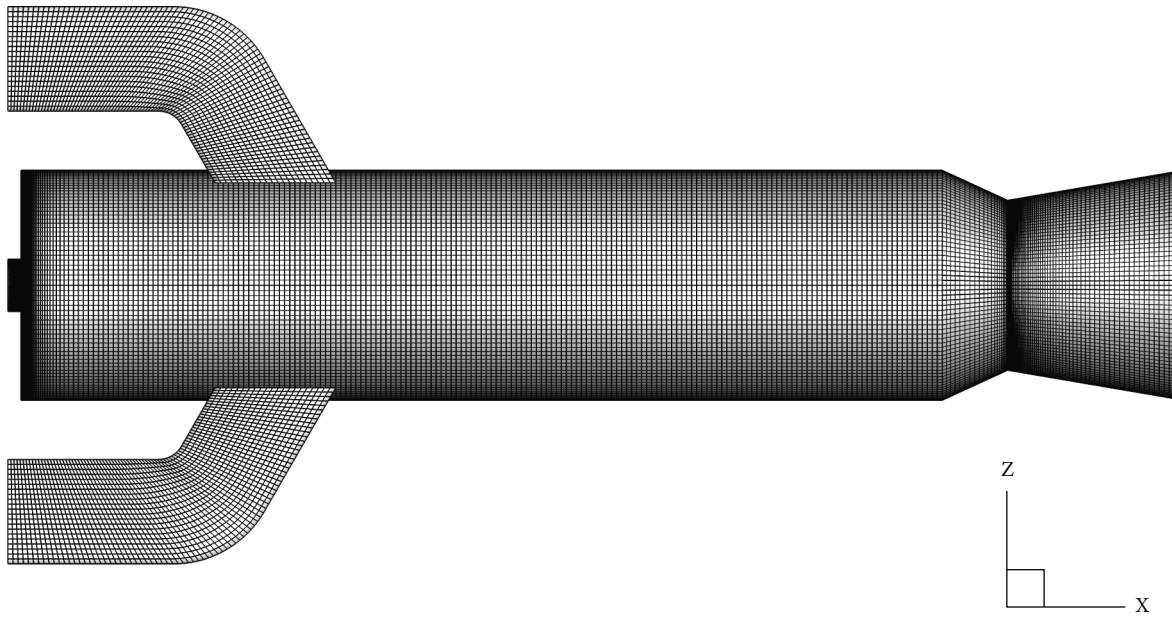


Figure 2: Grid applied in computational fluid dynamics.

*3.3. Boundary Conditions.* The simulated flight altitude is 20,000 meters above sea level, and the Mach number is 3.

Table 1 shows the boundary conditions in the study, which can be summarized as follows: (1) the mass flow inlet condition at the inlet and the entrance of the air inlet, (2) the pressure outlet at the outlet of the afterburner, and (3) the no-slip adiabatic wall condition at the inner wall.

*3.4. Characterization of Combustion Efficiency.* The component combustion completion rate, with clear physical meaning and simple calculation, was employed to calculate the combustion efficiency. The combustion efficiency of the gas phase component $i$ in any cross-section could be expressed by the following formula:

$$\eta_i = 1 - \frac{\int_A P_i \mu_i \omega_i dA}{\dot{m}_i}, \tag{7}$$

where $A$ is the integral section. $\eta_i$, $\rho_i$, $\mu_i$, and $\omega_i$ are the combustion efficiency, density, viscosity coefficient, and mass fraction of the gas phase component $i$ in the section, respectively. $\dot{m}_i$ is the total mass flow rate of component $i$.

The total combustion efficiency of the gas phase can be written as follows:

$$\eta_g = \frac{Q_{CO}\lambda_{CO}\eta_{CO} + Q_{H_2}\lambda_{H_2}\eta_H}{Q_{CO}\lambda_{CO} + Q_{H_2}\lambda_{H_2}}, \tag{8}$$

where $Q_{CO}$ is the combustion heat of CO. $Q_{H_2}$ is the combustion heat of $H_2$. $\lambda_{CO}$ is the mass percentage of CO, and $\lambda_{H_2}$ is the mass percentage of $H_2$ in the gas phase components.

The combustion efficiency of the boron particles in any cross section can be written as follows:

$$\eta_B = 1 - \frac{\int_A \dot{m}_B dA}{\dot{m}_{B,0}}, \tag{9}$$

where $\dot{m}_B$ is the mass flow rate of boron particles remaining on section A. $\dot{m}_{B,0}$ is the total mass flow rate of the boron particles.

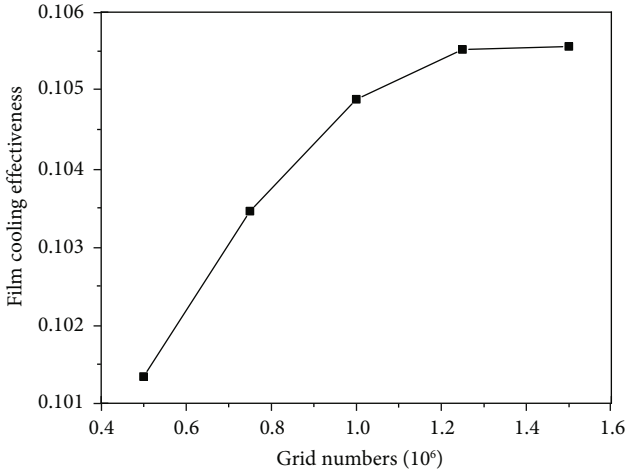


Figure 3: The film cooling effectiveness of the validation cases.

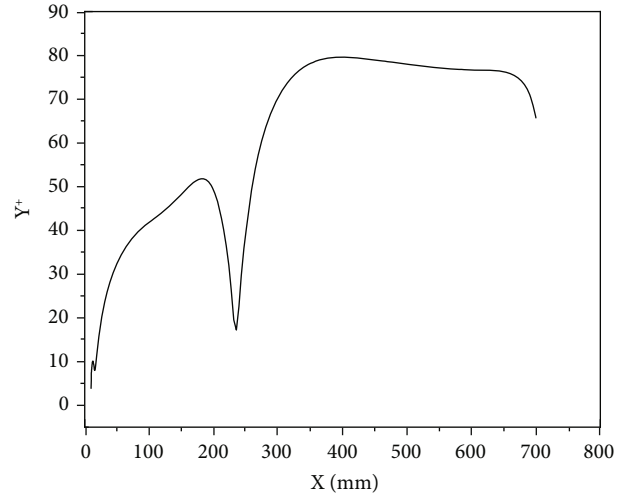


Figure 4: $y^+$ of case 2 with a grid number of 1.2 million.

The total combustion efficiency in any cross section can be written as follows:

$$\eta = \frac{\beta_g\left(Q_{CO}\lambda_{CO}\eta_{CO} + Q_{H_2}\lambda_{H_2}\eta_{H_2}\right) + \left(1-\beta_g\right)Q_B\eta_B}{\beta_g\left(Q_{CO}\lambda_{CO} + Q_{H_2}\lambda_{H_2}\right) + \left(1-\beta_g\right)Q_B}, \quad (10)$$

where $\beta_g$ is the mass percentage of the gas phase components and $Q_B$ is the combustion heat of boron.

*3.5. Grid Independency.* A multiblock grid approach was used to generate the computational domain [39]. The computational domain and grid were generated using the commercial software ICEM. The main part of the afterburner used a double O-grid. The grid was clustered near the wall boundary, the primary combustion inlet, and the powder inlet (see Figure 2). To save computing resources and guarantee the accuracy of the calculation, grid independence validation was conducted. As shown in Figure 3, the simulations with different grid numbers for case 2 were conducted. When the grid number was greater than 1.2 million, the grid number had little effect on the film cooling effectiveness of the wall, so the case with a grid number of 1.2 million (1236080) was used in this work. The height of the first row of cells was set at a distance of 0.1 mm for the inner walls. The $y^+$ of case 2 with a grid number of 1.2 million is shown in Figure 4. It can be seen from the figure that the $y^+$ values for the grid were controlled to be under the value of 100, which met the requirements of the standard $k$-$\varepsilon$ model.

*3.6. Model Validation.* Several experiments were carried out to validate the numerical models with the conditions of case 2 on a direct-connect test bed [40]. The experiment results, including the pressure on line 1 and the temperature at point 1 (as shown in Figure 5), were collected and compared with the simulation results. The result of the pressure is illustrated in Figure 6. The agreement between the simulation results and the experimental result from A-1 was found to be excellent. Table 2 shows the comparison of the temperature at point 1 between the four experimental results and the simulations. From the table, it can be seen that the absolute value of the temperature difference between the experimental results and the simulation result was controlled at about 100 K, and the deviation between the average temperature of the four experimental results and the simulation temperature was 5.36%. In summary, a good agreement was obtained for the simulation results and the experimental results, indicating that the simulation results in this research were accurate, and the calculation model was reliable.

## 4. Results and Discussion

*4.1. Temperature Distribution*

*4.1.1. Global Temperature Distribution.* To explore the effects of different air inlet angles on the combustion, Figure 5 shows the temperature distributions in each cross section of the afterburners. It can be seen from the figure that the global temperature of the internal flow field was axially symmetric. At the head of the afterburners, the temperature was high and even. From case 1 to case 4, the high temperature regions and the low temperature regions gradually shrank, and between the temperature regions, the transition tended to be smooth. This was likely because as the air inlet angle increased, the radial velocity of the ram air was improved, and the impact effect of the ram air on the primary gas was enhanced, causing the ram air at a low temperature and the primary gas at a high temperature to fully mix, so the temperature distribution in the afterburners was more even.

Figure 7 shows the oxygen concentration on the two marking lines on the inner wall of the afterburners. Line 1 passed through the high temperature region, and line 2 mainly passed through the low temperature region, as shown in Figure 5. It can be seen from the figure that the oxygen concentration on line 2 was three orders of magnitude greater than that on line 1, indicating that oxygen was mainly concentrated in the low temperature regions. From case 1 to case 4, the oxygen concentration on line 2 gradually

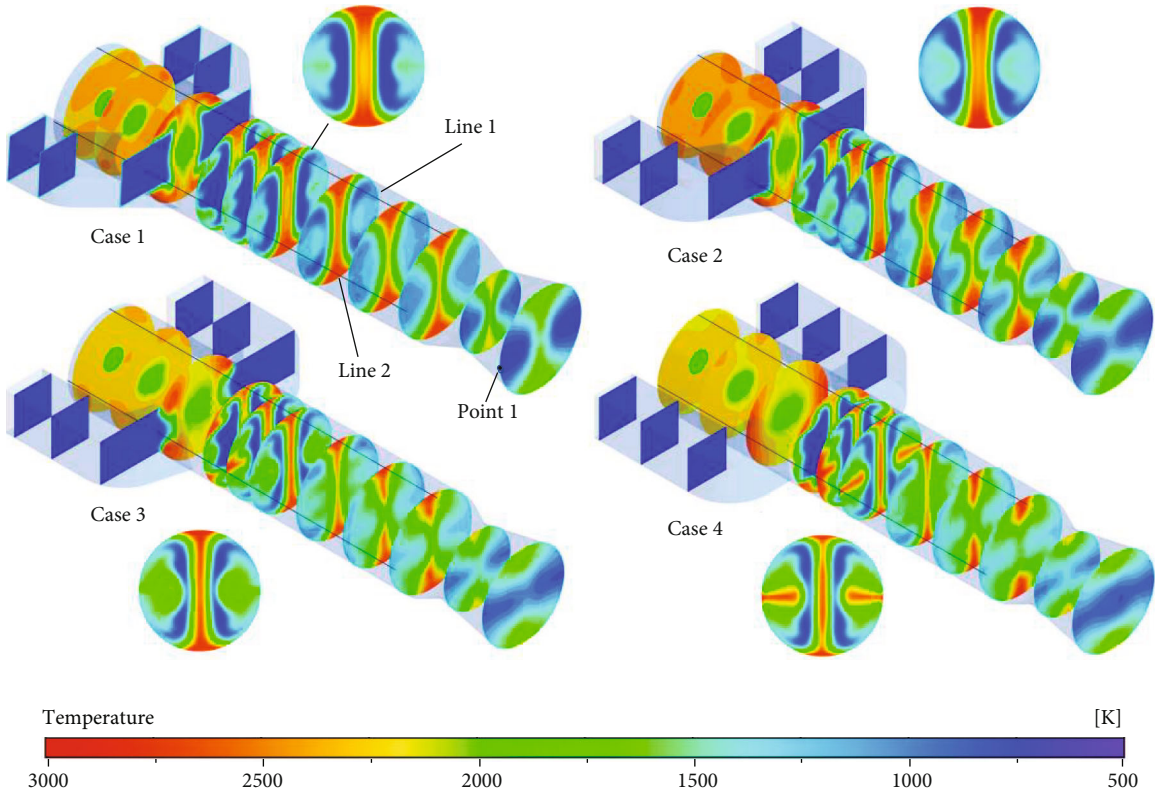


Figure 5: Temperature distributions in each cross section of the afterburners, shown individually in the cross section of $x = 400$ mm.

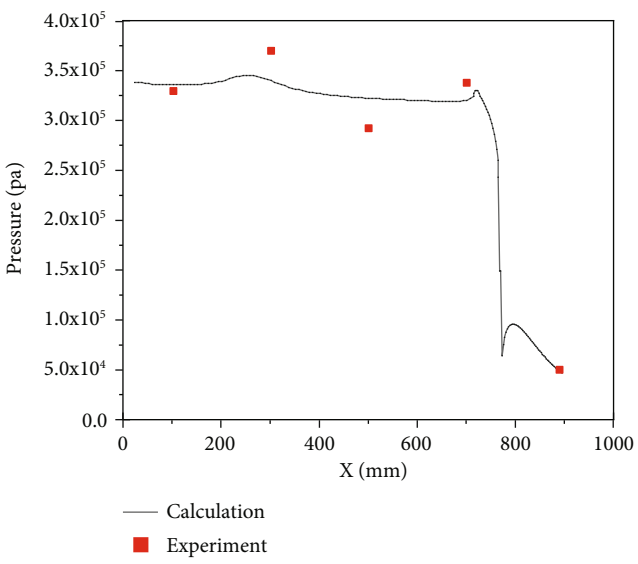


Figure 6: Comparison of pressure on line 1 for the simulation and experiment A-1.

decreased from 19.1% in case 1 to 16.8% in case 4 behind the air inlet exits (500 mm < $x$ < 800 mm), while the oxygen concentration on line 1 increased. Therefore, it could be seen that the oxygen concentration decreased in the low temperature regions and increased in the high temperature regions, showing that the distribution of oxygen in the afterburners tended to be even as the air inlet angle increased.

The streamlines of the primary gas and the air are shown in Figure 8 to explore the reasons for the above temperature distribution and the oxygen distribution. It is shown in the figure that behind the air inlet exits, the primary gas was concentrated near the axis of the afterburners, while the air was mainly concentrated near the wall. From case 1 to case 4, the air streamlines and the primary gas streamlines were more interleaved, and the primary gas streamlines tended to diverge. All of these factors indicated that as the air inlet angle increased, the impact effect of the ram air on the primary gas was enhanced, causing the primary gas and the ram air to be fully mixed, so the distribution of the primary gas and air in the afterburner was more even, which was why the temperature and the oxygen in the afterburners showed the above distribution.

*4.1.2. Local Temperature Distribution near the Outlet of the Air Inlets.* Figure 5 shows that the local temperature distribution near the air inlet exits was also significantly affected by different air inlet angles (see the temperature distribution in the cross section of $x = 400$ mm). To further explore this phenomenon, Figure 9 shows the temperature distribution on the axial symmetrical sections of the afterburners, from which it can be seen that as the air inlet angle increased, larger local high temperature areas appeared near the air inlet exits, and the maximum temperatures were improved. For example, the maximum temperatures reached 1400 K, 1700 K, 2700 K, and 2900 K from case 1 to case 4.

Table 2: Comparison of temperature at point 1 for the simulation and experiments.

| Experiment | A-1 | A-2 | A-3 | A-4 | Average temperature/K | Case 2 calculation temperature/K | Deviation |
|---|---|---|---|---|---|---|---|
| Temperature/K | 671 | 594 | 565 | 707 | 634.3 | 602 | 5.36% |

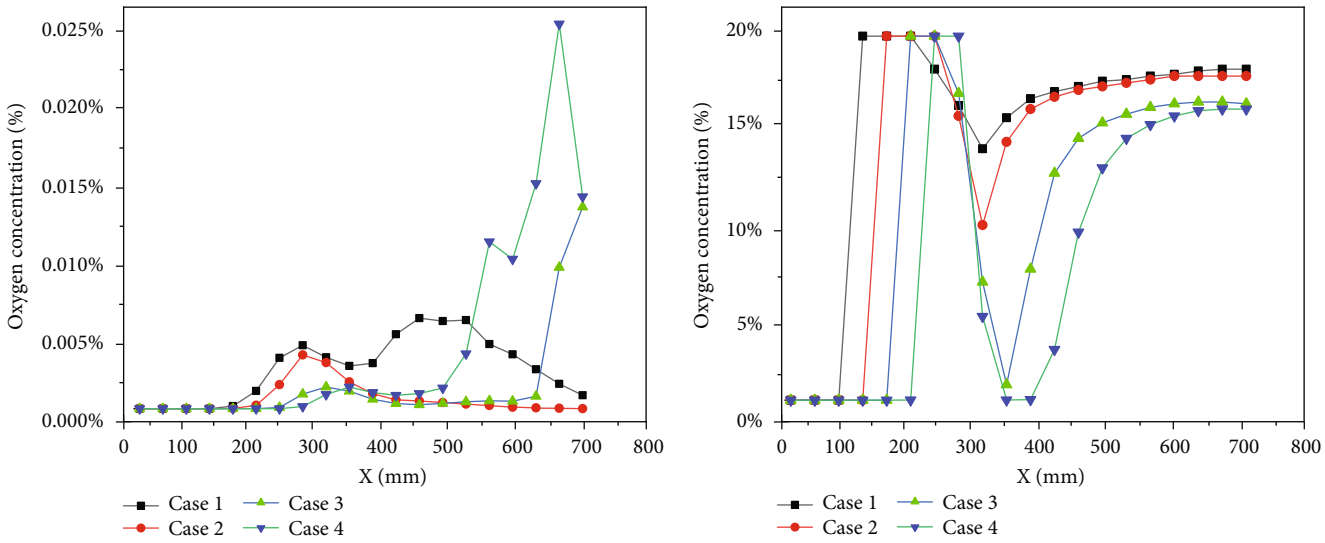


(a) Oxygen concentration on line 1

(b) Oxygen concentration on line 2

Figure 7: Oxygen concentration on two marking lines.

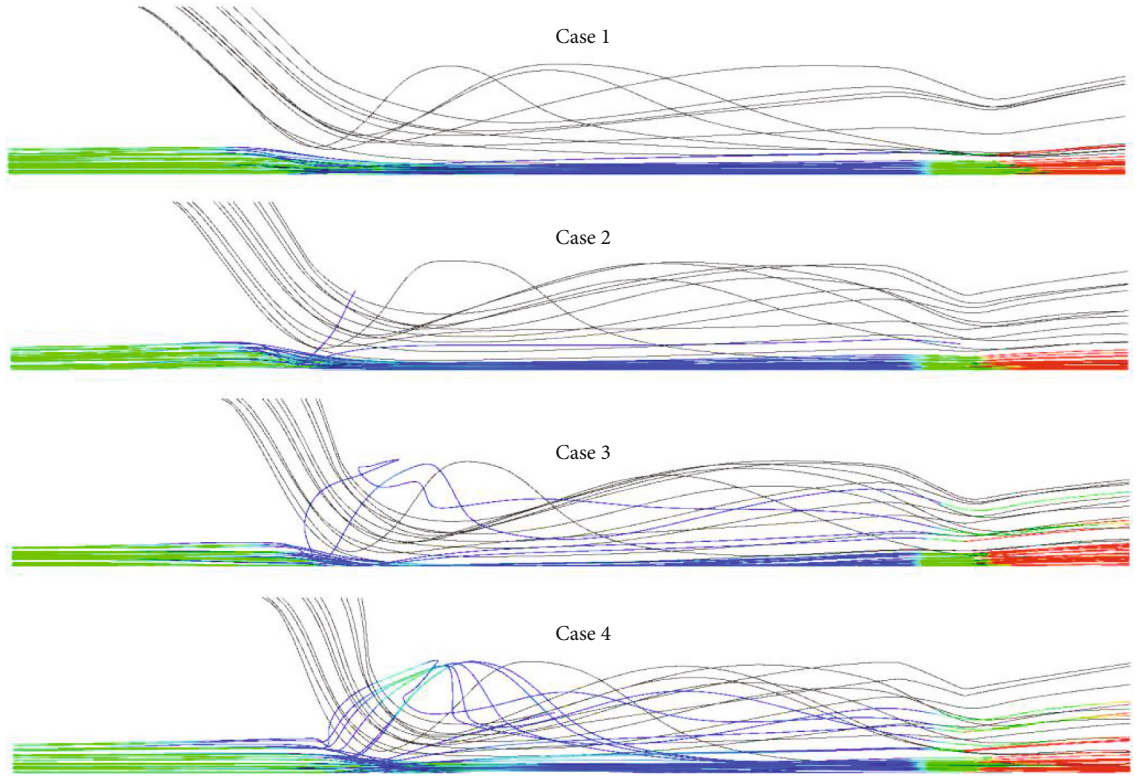


Figure 8: Streamlines of primary gas and air.

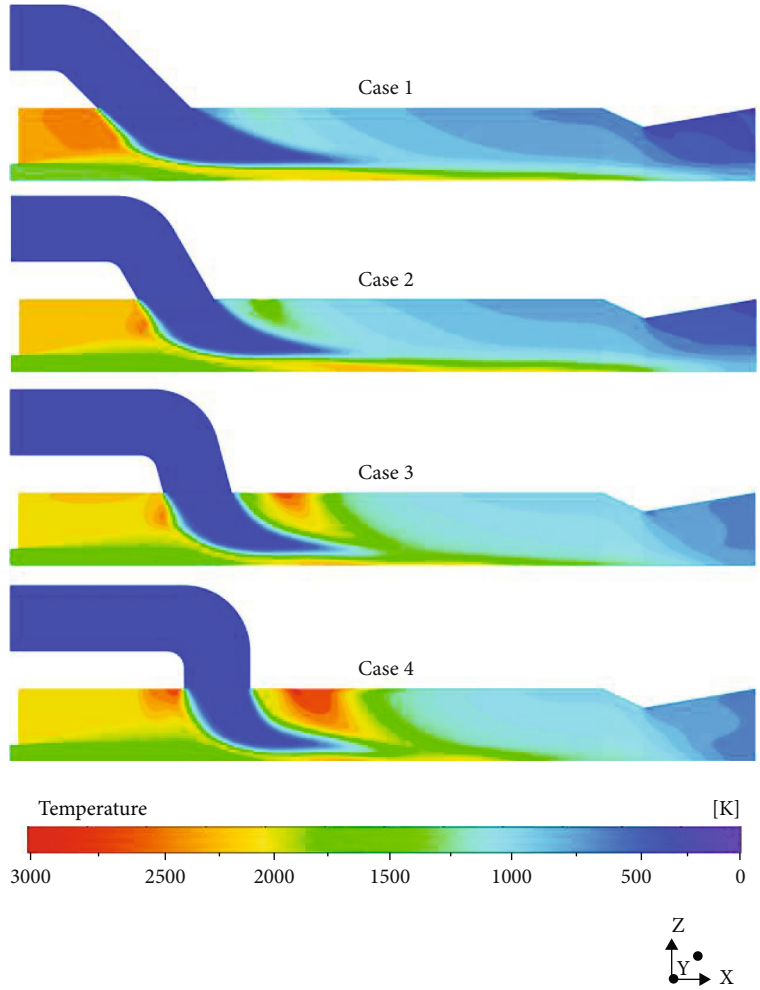


Figure 9: Temperature distribution on axial symmetrical sections of afterburners.

For the sake of the analysis of the above local temperature distribution, Figure 10 shows the velocity vector on the front sides of exits. As the air inlet angle increased, the number of local vortices increased from one to two, and their range also extended. The $x = 350$ mm section behind the air inlet exits was selected. Its velocity vector is shown in Figure 11. From case 1 to case 4, it can be seen that the local single vortex extended to double vortices with larger ranges. This was because as the air inlet angle increased, the radial velocity of the ram air was accelerated, enhancing the impact between the ram air and the combustion gas in regions near the air inlet exits, so the local vortexes become more intense, and the mixing combustion was strengthened. Therefore, it could be concluded that as the air inlet angle increases, a larger range and a greater intensity of the local vortices were generated on both sides of the air inlet exits. Therefore, the mixed combustion of primary gas and oxygen at those locations was enhanced, resulting in the above local high temperature area.

*4.2. Combustion Efficiency.* To explore the effect of different air inlet angles on the combustion efficiency of the afterburners, the gas-phase combustion efficiency, the boron particle combustion efficiency, and the total combustion efficiency in each cross section were calculated in this work. The changes in the gas-phase combustion efficiency in each cross section for different cases can be seen in Figure 12. The gas-phase combustion efficiency in the nozzle outlet section ($x = 900$ mm) could reach more than 99% for the four cases, indicating that for this kind of afterburner with symmetrical air inlets, the combustion of the primary gas was completed, and different air inlet angles had little effect on the combustion efficiency of the gas-phase components.

Figure 13 shows the changes in the combustion efficiency of the boron particles in each cross section in different cases. The boron particle combustion efficiency order in the four cases from high to low was $\eta_{B75^\circ} > \eta_{B90^\circ} > \eta_{B60^\circ} > \eta_{B45^\circ}$, where $\eta_{B75^\circ} = 53.73\%$, $\eta_{B90^\circ} = 50.54\%$, $\eta_{B60^\circ} = 46.09\%$, and $\eta_{B45^\circ} = 42.51\%$. The total combustion efficiency order of each cross section in the four cases can be seen in Figure 14, which from high to low was $\eta_{75^\circ} > \eta_{90^\circ} > \eta_{60^\circ} > \eta_{45^\circ}$, where $\eta_{75^\circ} = 84.34\%$, $\eta_{90^\circ} = 83.26\%$, $\eta_{60^\circ} = 81.64\%$, and $\eta_{45^\circ} = 80.38\%$. In comparison, the changing trend of the total combustion efficiency was similar to that of the boron particle combustion efficiency. Thus, it could be inferred that as the air inlet angle changed, the total combustion efficiency

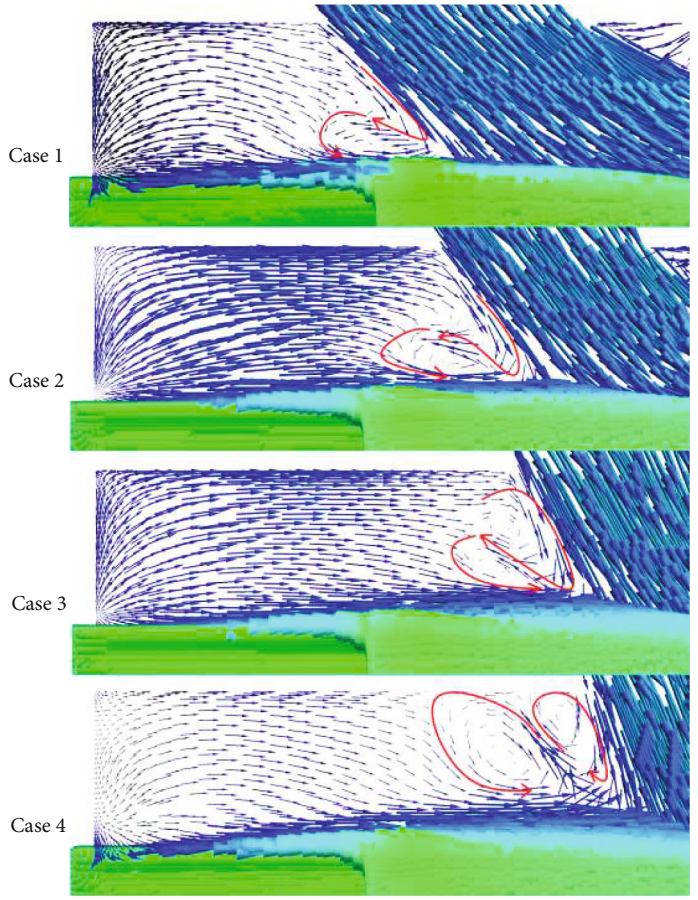


Figure 10: The velocity vector in the front side of the air inlet exits.

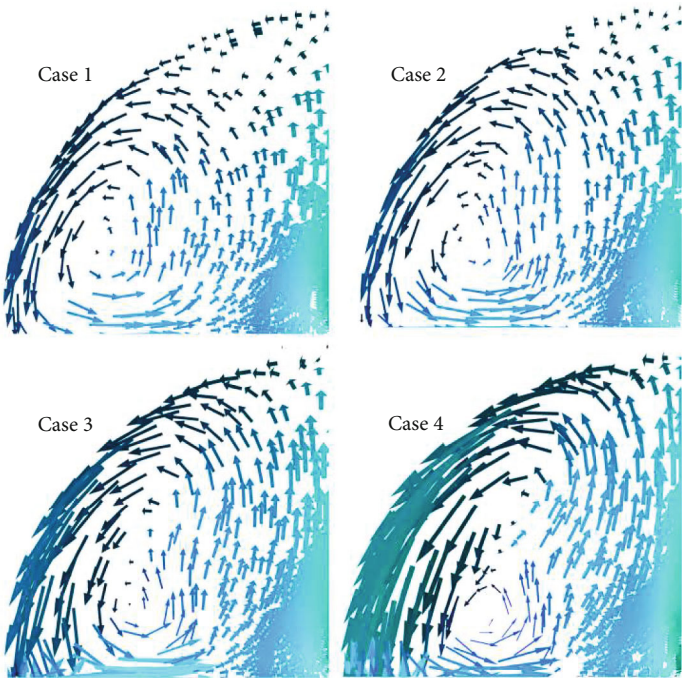


Figure 11: The velocity vector in the section of $x = 350$ mm. The section was at the back side of the air inlet exits.

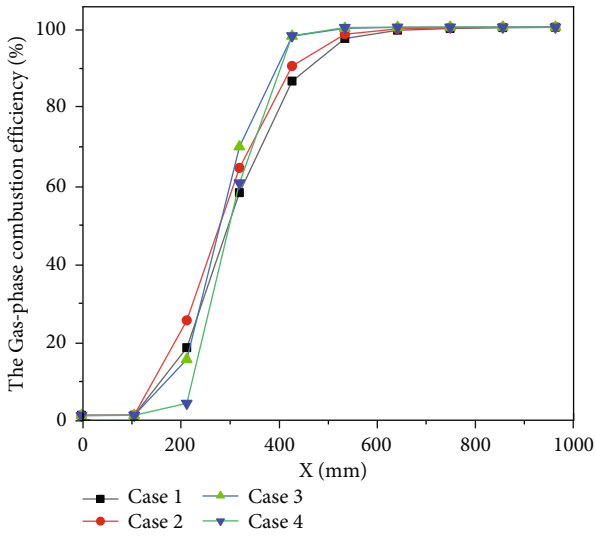


Figure 12: The gas-phase combustion efficiency in each cross section of the afterburners.

was mainly determined by the boron particle combustion efficiency, both of which first increased (from 45° to 75°) and then decreased (from 75° to 90°).

A further study of the boron particle combustion efficiency was carried out. This combustion efficiency is usually determined by factors such as temperature, oxygen concentration, and boron particle residence time in the afterburner [41, 42].

Figure 15 shows the trajectories of the boron particles in the afterburner, which were closely related to the residence time of the boron particles. It can be seen from the figure that the boron particles were mainly concentrated on the head regions of the afterburners and the axial planes of the symmetry of afterburners. In combination with the analysis of the oxygen distribution described in Section 4.1.1, the oxygen concentration in these regions was low where the boron particles were dense. Therefore, it could be considered that the change in the boron particle combustion efficiency was not mainly caused by the change in the oxygen concentration. From case 1 to case 4, the trajectories of the boron particles at the head of the afterburners and near the air inlet exits tended to be dense, and the average residence time was also longer. Combined with the analysis described in Section 4.1.2, it could be inferred that as the air inlet angle increased, the vortexes in the regions of the afterburner heads and near the air inlet exits were enhanced, making more boron particles gather in these regions and move with the vortexes, thus prolonging the residence time of the boron particles in the afterburners.

In addition to the boron particle residence time, the effect of the environment temperature on the boron particle combustion efficiency was investigated in this work, as shown in Figure 16. It can be seen from the figure that from case 1 to case 4, the high temperature region greater than 2600 K in the afterburner first expanded (from 45° to 60°) and then shrank (from 75° to 90°). This was because as the air inlet angle increased, the radial velocity of the ram air increased, which strengthened the mixing between the ram air and the primary gas, enhancing the combustion and rising global temperature in the afterburners. However, when the air inlet increased to a critical value (in this work, the increase was from 60° to 75°), the ram air with a cold temperature squeezed the high temperature combustion gas in the afterburners, and this effect was stronger than the mixing effect caused by ram air, leading to the concentration of the high temperature regions in a narrow range near Line 1 behind the air inlet exits, causing the reduction of the high temperature regions. Combined with the change tendency of the boron particle combustion efficiency in four cases, we inferred that the boron particle combustion efficiency was increased because of the larger high temperature region. When the high temperature region shrank, it led to the reduction of the combustion efficiency.

In summary, increasing the air inlet angle had little effect on the gas-phase combustion efficiency, but it could lead to the boron particle combustion efficiency first increasing and then decreasing. Consequently, the residence time of the boron particles increased, and the high temperature region expanded first as the air inlet angle increased, both of which promoted the combustion efficiency of the boron particles. However, when the angle reached 75°, although the boron particle residence time continued to be prolonged, the high temperature region shrank, which became the dominant factor and reduced the boron particle combustion efficiency. Since the total combustion efficiency was mainly determined by the boron particle combustion efficiency, the total combustion efficiency also had a similar tendency to first increase and then decrease. When the air inlet angle was 75°, the total combustion efficiency was the highest, reaching 84.34%.

*4.3. Inner Wall Flow Field.* The insulation layer of an afterburner is generally made of composite materials such as silicon rubber, undergoing intense thermal decomposition at a high temperature and serious oxidation, which is closely related to the environment temperature, so it is important to analyze the temperature distribution of the afterburner inner wall. In addition, in a real work environment, the insulation layer is also resistant to severe particle erosion and airflow scouring, which causes the main damage to the afterburner insulation layer [43]. Therefore, in this work, the ablation conditions of the afterburner insulation layer were studied by analyzing the temperature distribution, oxygen concentration, airflow scouring, and erosion of the condensed phase particles of the inner wall [44].

According to Figure 5, the whole afterburner inner wall could be divided into a high temperature wall and a low temperature wall, and line 1 passed through the whole high temperature inner wall, while line 2 went through the main part of the low temperature inner wall. The characteristics of the inner wall were analyzed by studying the parameter distribution on the two making lines. Figure 17 shows the temperature change on the two marking lines. It can be seen from the figure that the temperature on line 1 for the four cases varied from 2300 K to 2900 K. The value range change was smaller than that on line 2, and the temperature difference

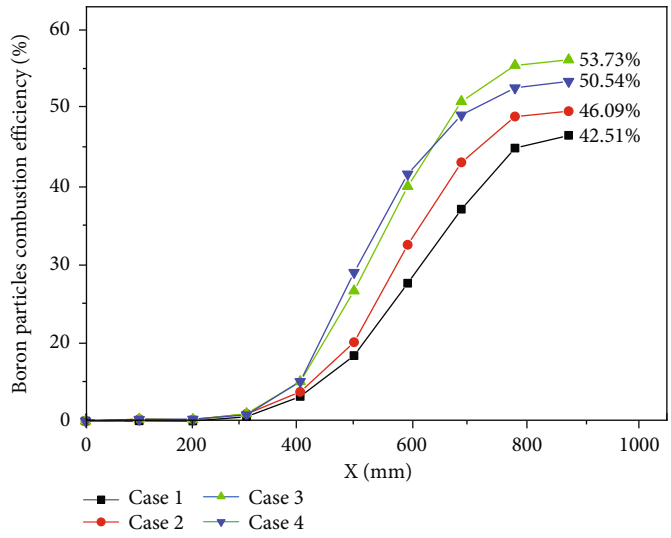


Figure 13: Boron particle combustion efficiency in each cross section of afterburners.

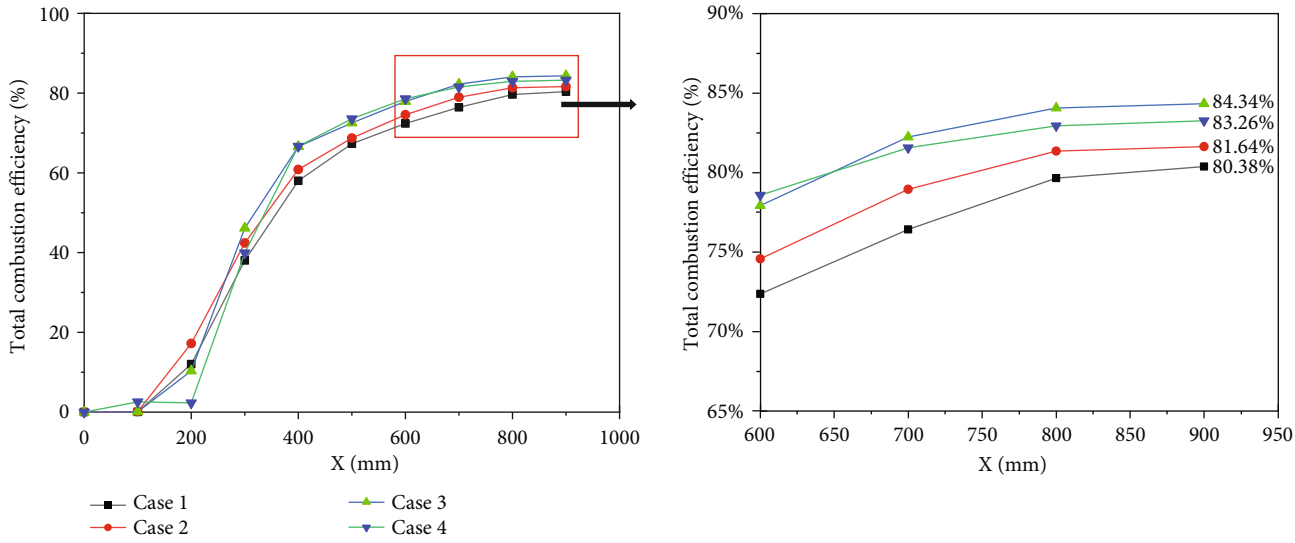


Figure 14: Total combustion efficiency in each cross section of afterburners.

at the same position of the $X$ coordinate for different cases was small. Combined with Figure 7, the oxygen concentration on line 1 had only a slight change, from 0.005% in case 1 to 0.020% in case 4. This indicated that the change of the air inlet angle had little influence on the high-temperature inner wall. However, for the temperature distribution on line 2, there was a maximum temperature after $x = 300$ mm, and it gradually rose from case 1 to case 4, at 1447 K in case 1, 1734 K in case 2, 2763 K in case 3, and 2851 K in case 4. Combined with the analysis described in Section 4.1.2, it could be inferred that as the air inlet angle increased, the radial velocity of the ram air increased, leading to a more severe impact between the ram air and the combustion gas, generating a larger range and more intense vortexes behind the air inlet exits (from $x = 300$ to $x = 450$ mm), so the mixing combustion there was enhanced and the temperature increased. Therefore, as the air inlet angle increased, some influences affected the low temperature inner wall because the temperature of the local inner wall behind the air inlet exits rose, gradually causing a great temperature gradient. Due to the different thermal strain rates of the thermal protection materials, a concentration of the thermal stress was caused, likely leading to crack formation in the insulation layer, which was not conducive to thermal protection.

To explore the airflow scouring effect on the afterburner inner wall, the velocity distributions on two marking lines were calculated, as seen in Figure 18. It can be seen from the figure that behind the air inlet exits (from $x = 300$ mm to $x = 600$ mm), the airflow velocities on line 1 and line 2 all increased from case 1 to case 4, and the maximum velocities on line 1 and line 2 for case 4 reached 380 m/s and 220 m/s, respectively. The squeezing effect of the ram air

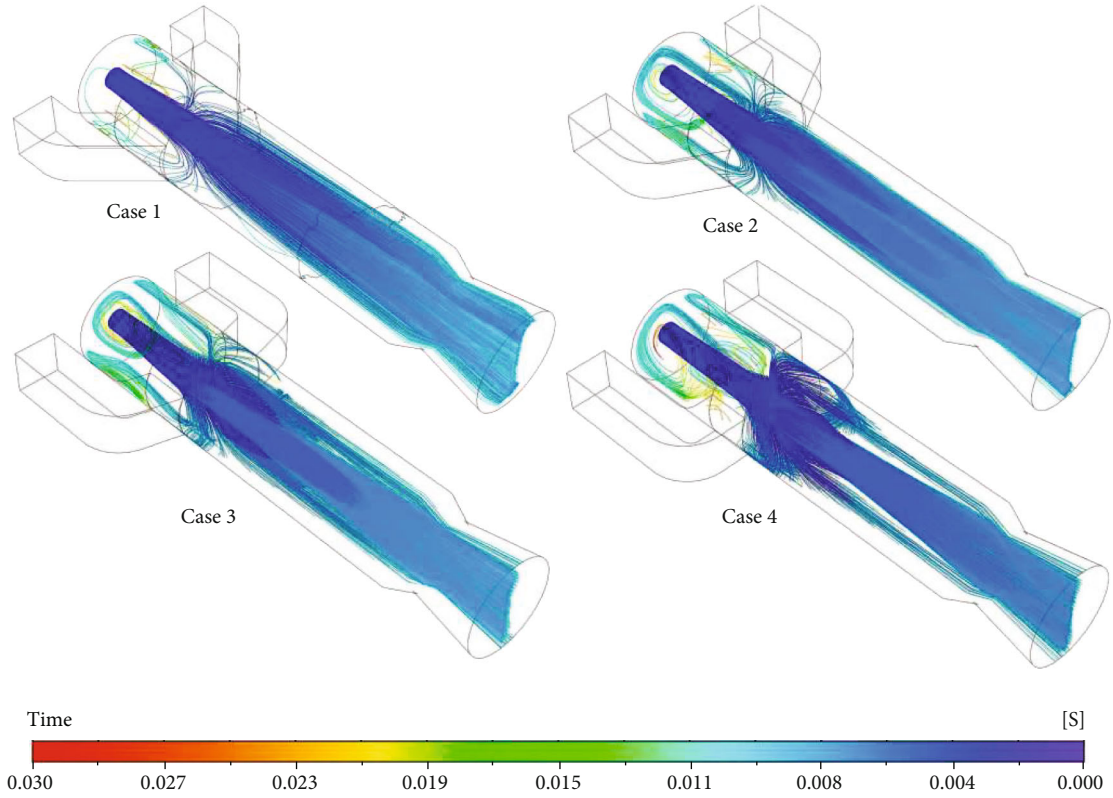


Figure 15: The trajectories of the boron particles were mainly concentrated on the regions of afterburner heads and the axial planes of symmetry. The vortexes in the heads of the afterburners and near the air inlet exits were enhanced.

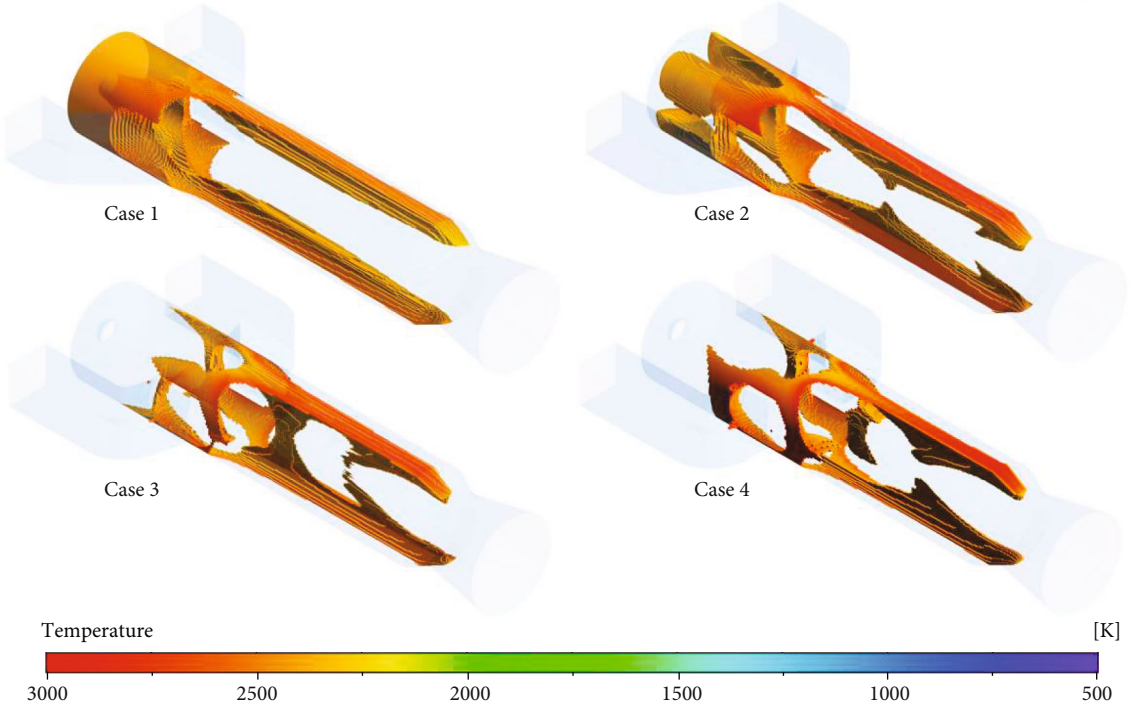


Figure 16: The regions with temperatures greater than 2600 K in the afterburners.

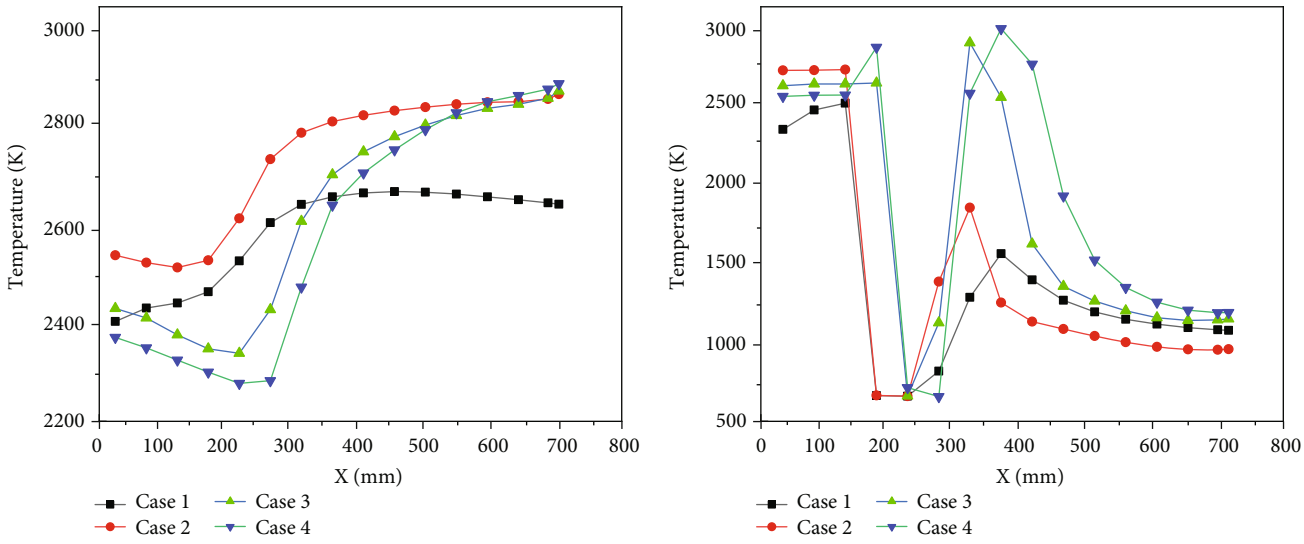


(a) Temperature distribution on line 1

(b) Temperature distribution on line 2

Figure 17: Temperature distribution on two marking lines. Line 1 is on the high temperature wall, while line 2 is on the low one.

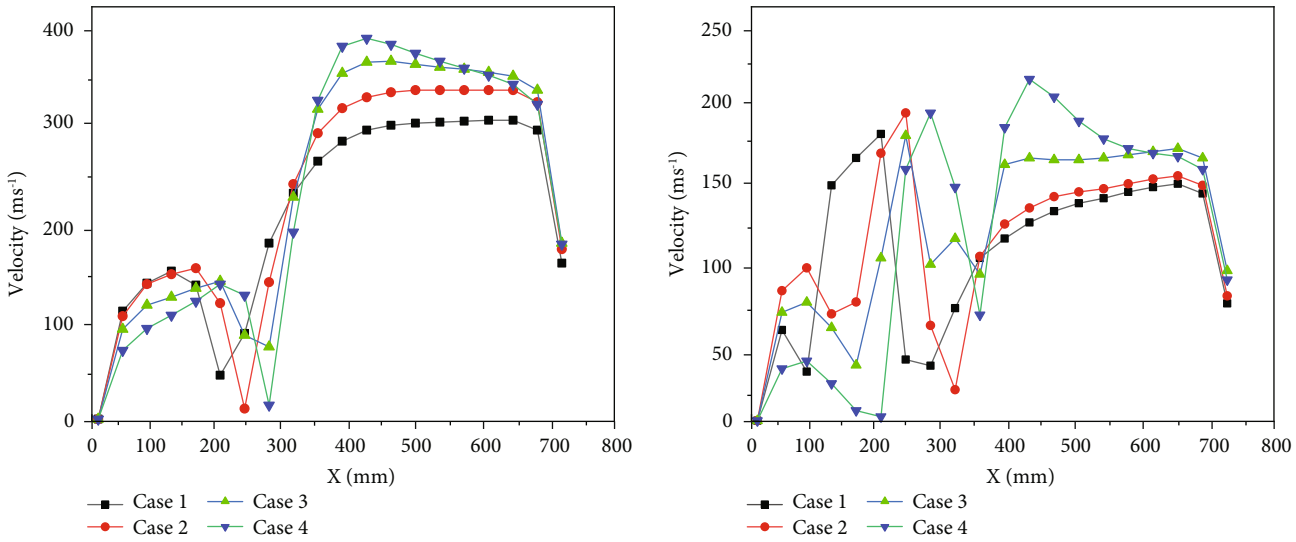


(a) Velocity distribution on line 1

(b) Velocity distribution on line 2

Figure 18: Velocity distribution on two marking lines.

on the combustion gas was enhanced because of the increase of the air inlet angle, which let the combustion gas concentrate in the region near the inner wall so that the velocity on the two lines increased. Some researchers believe that for the high temperature jet in a rocket engine combustion chamber, the shearing effect of the high temperature jet on the thermal insulation material surface is the main reason why the material is ablated and damaged, and the effect is severe as the velocity of jet increases [45, 46]. Therefore, it could be determined that as the air inlet angle increased, the airflow velocity on the afterburner inner wall behind the air inlet exits increased, which intensified the airflow scouring on the inner wall.

The density distribution on the two lines was also calculated to study the erosion effect of the condensed phase particles on the inner wall in this work (see Figure 19). It can be seen from the figure that behind the air inlet exits (from $x = 300$ mm to $x = 600$ mm), the density on line 1 increased from case 1 to case 4, with increases of 0.365 kg/m$^3$ in case 1, 0.358 kg/m$^3$ in case 2, 0.374 kg/m$^3$ in case 3, and 0.381 kg/m$^3$ in case 4, indicating that a larger number of condensed phase particles were collected on the high temperature wall surface by the flow. This was because the stronger squeezing effect of the ram air on the primary gas with boron particles made the particles concentrate in the regions near the high temperature wall. On line 2, although

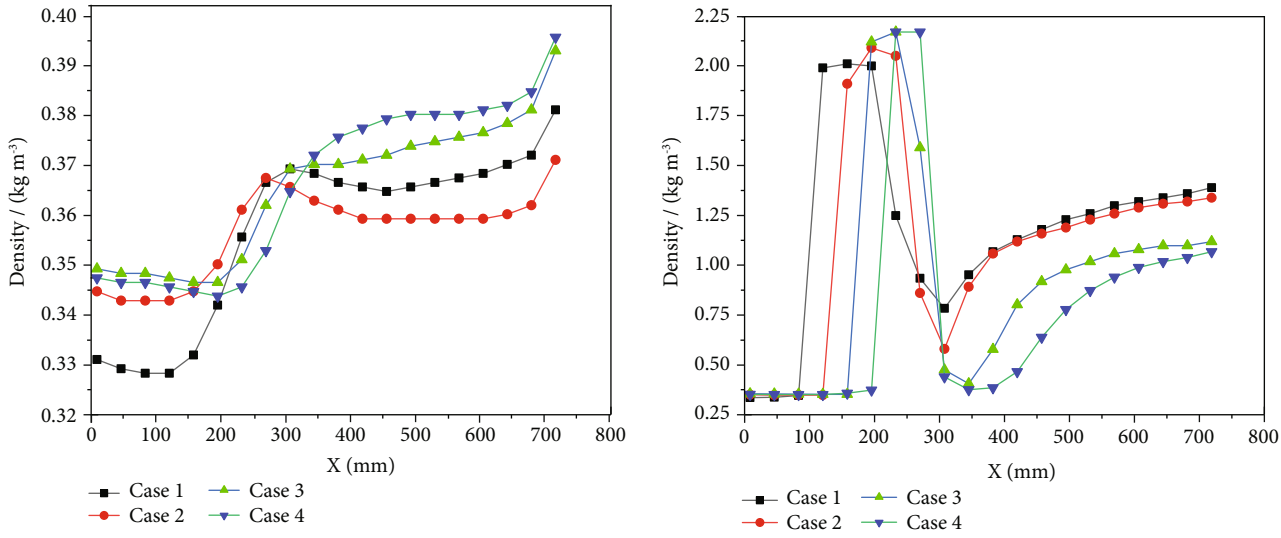


(a) Density distribution on line 1

(b) Density distribution on line 2

Figure 19: Density distribution on two marking lines.

the density on line 2 was about an order of magnitude larger than that on line 1, as seen in Figures 15 and 16, the temperature on the low temperature wall mostly did not exceed 1200 K, and the velocity was low, approximately 100 m/s. Therefore, the condensed phase particles had little erosion effect on the inner wall [47]. In conclusion, with the increase of the air inlet angle, it could be concluded that the erosion effect of the condensed phase particles on the inner wall increased on the high temperature wall, but there was little change on the low temperature wall.

In summary, as the air inlet angle increased, the overall jet environment of the inner wall tended to be harsh. For the high temperature wall, the erosion effect of the condensed particles on the inner wall behind the air inlet exits increased; for the low temperature wall, the large temperature gradient was generated on the inner wall near air inlet exits, which meant that the thermal insulation layer tended to crack. The whole inner wall sustained a notable airflow scouring effect because of the accelerated combustion gas flow.

## 5. Conclusions

In this study, a hybrid powder-solid ramjet (HPSR) with symmetrical air inlets was investigated. The two-phase flow and the combustion in the afterburners were numerically simulated based on King's boron particle ignition and combustion model, a standard $k$ - $\varepsilon$ model, and an eddy-dissipation model (EDM). The effects of different air inlet angles on the combustion efficiency and the inner wall ablation were evaluated. According to the results, as the air inlet angle increased, the following conclusions were drawn:

(i) The impact of the ram air on the primary fuel gas was enhanced, and the mixing between the primary gas and the ram air was more thorough, which resulted in the distributions of the temperature and the oxygen tending to be more even

(ii) Vortices with higher intensity and a larger range were gradually generated near the air inlet exits, which enhanced the mixing combustion of the primary gas and oxygen there, resulting in local high temperature regions

(iii) The boron particle combustion efficiency and the total combustion efficiency first increased and then decreased as the air inlet angle changed. There was an optimal air inlet angle to maximize the total combustion efficiency from 60° to 90° in this work. The total combustion efficiencies of the afterburner were 80.38%, 81.64%, 84.34%, and 83.26% for air inlet angles of 45°, 60°, 75°, and 90°, respectively

(iv) The global jet environment in the afterburners was more severe. For the high temperature wall, the erosion of condensed phase particles was enhanced, intensifying the comprehensive damage to the wall; for the low temperature wall, a large temperature gradient was generated near the air inlet exits, in that the thermal insulation layer tended to be cracked there. The gas-flow scouring effect on the inner wall was enhanced in the whole afterburner inner wall

(v) When designing the air inlet angle, the total combustion efficiency and the inner wall thermal protection had to be considered comprehensively. It was better to set the air inlet angle between 60° and 75°, which could improve the total combustion efficiency while reducing the difficulty of the thermal protection of the inner wall

## Nomenclature

$x$: $X$ direction
$y$: $Y$ direction

$z$: $Z$ direction
$t$: Time (s)
%: Mass fraction of the components
$\theta$: Air inlet angle
**Q**: Conservative vectors
**F**: Vectors of convective flux
**G**: Vectors of viscous flux
**H**: Vectors of source terms
$u_p$: Velocity of particles (m/s)
$\rho_p$: Density of particle (kg/m$^3$)
$u$: Velocity of fluid (m/s)
$\rho$: Density of fluid (kg/m$^3$)
$d_p$: Particle diameter (m)
$\delta$: Oxide layer thickness of particle (m)
$T_p$: Particle temperature (K)
$\dot{Q}$: Heat fluxes (w/m$^2$)
$R$: Reaction rate (kg/s)
M: Molar mass
$c_p$: Specific heat (J/(kg·K))
$P_i$: Partial pressure of component $i$ (Pa)
$\eta_i$: Combustion efficiency of component $i$
$\rho_i$: Density of component $i$ (kg/m$^3$)
$\omega_i$: Mass fraction of component $i$
$\mu_i$: Viscosity of component $i$ (Pa·s)
$\dot{m}_p$: Burning rate of particle (kg/s)
$\dot{m}_i$: Total mass flow rate of component $i$ (kg/s)
$\eta_g$: The combustion efficiency of gas phase
$Q_i$: Combustion heat of component $i$ (J/mol)
$\lambda_i$: Mass fraction of component $i$ in the gas phase.

## Data Availability

Some or all of the data, models, or code generated or used during the study are available from the corresponding author by request.

## Conflicts of Interest

The authors declare that they have no conflict of interest.

## Acknowledgments

The financial support from the National Natural Science Foundation of China (52003296), the Nature Science Basic Research Program of Shaanxi Province (2020JQ-488), and the Key Laboratory Foundation of Shaanxi Province (2019SZS-09) is gratefully acknowledged. We thank LetPub (http://www.letpub.com) for its linguistic assistance during the preparation of this manuscript.

## References

[1] H. Besser, "History of ducted rocket development at Bayern-Chemie," in *44th AIAA/ASME/SAE/ASEE Joint Propulsion Conference & Exhibit*, p. 5261, Hartford,CT, 2008.

[2] P. J. Waltrup, M. E. White, F. Zarlingo, and E. S. Gravlin, "History of U.S. Navy ramjet, scramjet, and mixed-cycle propulsion development," *Journal of Propulsion and Power*, vol. 18, no. 1, pp. 14–27, 2002.

[3] R. S. Fry, "A century of ramjet propulsion technology evolution," *Journal of Propulsion and Power*, vol. 20, no. 1, pp. 27–58, 2004.

[4] P. Hewitt, "Status of ramjet programs in the United States," *44th AIAA/ASME/SAE/ASEE Joint Propulsion Conference & Exhibit*, 2008, p. 5265, 2008.

[5] F. Dijkstra, A. Mayer, K. Wilson, R. Smith, and K. Schadow, "Ducted rocket combustion experiments at low gas-generator combustion temperatures," in *31st Joint Propulsion Conference and Exhibit*, p. 2415, San Diego,CA,U.S.A, 1995.

[6] G. Kurth, C. Bauer, and N. Hopfe, "Performance assessment for a throttleable ducted rocket powered lower tier interceptor," in *51st AIAA/SAE/ASEE Joint Propulsion Conference*, p. 4234, Orlando, FL, 2015.

[7] A. N. T. JR, "Some fundamental aspects of ramjet propulsion," *Journal of Jet Propulsion*, vol. 27, no. 4, pp. 381–385, 1957.

[8] G. Schulte, R. Pein, and A. Hogl, "Temperature and concentration measurements in a solid fuel ramjet combustion chamber," *Journal of Propulsion and Power*, vol. 3, no. 2, pp. 114–120, 1987.

[9] J. Chang, B. Li, W. Bao, W. Niu, and D. Yu, "Thrust control system design of ducted rockets," *Acta Astronautica*, vol. 69, no. 1-2, pp. 86–95, 2011.

[10] W. Jung, Y. Yun, K.-S. Kim, J. Park, and S. Kwon, "Performance evaluation of ramjet fuel grains with boron and magnesium additives," in *2018 Joint Propulsion Conference*, p. 4873, Cincinnati, Ohio, 2018.

[11] T. Mitani and M. Izumikawa, "Combustion efficiencies of aluminum and boron in solid propellants," *Journal of Spacecraft and Rockets*, vol. 28, no. 1, pp. 79–84, 1991.

[12] C. Li, C. Hu, X. Xin, Y. Li, and H. Sun, "Experimental study on the operation characteristics of aluminum powder fueled ramjet," *Acta Astronautica*, vol. 129, pp. 74–81, 2016.

[13] W. Jung, S. Baek, J. Park, and S. Kwon, "Combustion characteristics of ramjet fuel grains with boron and aluminum additives," *Journal of Propulsion and Power*, vol. 34, no. 4, pp. 1070–1079, 2018.

[14] U. Vellaisamy and S. Biswas, "Effect of metal additives on neutralization and characteristics of AP/HTPB solid propellants," *Combustion and Flame*, vol. 221, pp. 326–337, 2020.

[15] T. Odawara, M. Tanabe, and T. Kuwahara, "Ignition characteristics of boron particles in ducted rockets," in *41st AIAA/ASME/SAE/ASEE Joint Propulsion Conference & Exhibit*, p. 4498, Tucson, Arizona, 2005.

[16] B. Natan and A. Gany, "Ignition and combustion of boron particles in the flowfield of a solid fuel ramjet," *Journal of Propulsion and Power*, vol. 7, no. 1, pp. 37–43, 1991.

[17] A. Gany, "Thermodynamic limitation on boron energy realization in ramjet propulsion," *Acta Astronautica*, vol. 98, pp. 128–132, 2014.

[18] D. Liu, Z. Xia, L. Huang, and H. Jianxin, "Boron particle combustion in solid rocket ramjets," *Journal of Aerospace Engineering*, vol. 28, article 04014112, 2014.

[19] S. Alay Hashim, S. Karmakar, and A. Roy, "Combustion characteristics of boron-HTPB-based solid fuels for hybrid gas generator in ducted rocket applications," *Combustion Science and Technology*, vol. 191, pp. 1–19, 2018.

[20] Y. Xu, R. Jia, H. Medina, and H. Sun, "Effect of tangential swirl air inlet angle on the combustion efficiency of a hybrid

powder-solid ramjet," *Acta Astronautica*, vol. 159, pp. 87–95, 2019.

[21] R. Zvuloni, A. Gany, and Y. Levy, "Geometric effects on the combustion in solid fuel ramjets," *Journal of Propulsion and Power*, vol. 5, no. 1, pp. 32–37, 1989.

[22] C. Vigot, A. Cochet, and C. Guin, "Combustion behavior of boron-based solid propellants in a ducted rocket," *International Journal of Energetic Materials & Chemical Propulsion*, vol. 2, no. 1-6, pp. 386–401, 1991.

[23] R. Pein and F. Vinnemeier, "Swirl and fuel composition effects on boron combustion in solid-fuelramjets," *Journal of Propulsion and Power*, vol. 8, no. 3, pp. 609–614, 1992.

[24] S. Liu, J. Li, G. Zhu, W. Wang, and Y. Liu, "Mixing and combustion enhancement of turbocharged solid propellant ramjet," *Acta Astronautica*, vol. 143, pp. 193–202, 2018.

[25] O. Musa, L. Weixuan, C. Xiong, G. Lunkun, and L. Wenhe, "Experimental investigation on the effect of swirling flow on combustion characteristics and performance of solid fuel ramjet," *Acta Astronautica*, vol. 148, pp. 163–174, 2018.

[26] W. Li, D. Zhao, X. Chen, L. Zhu, and S. Ni, "Numerical investigation of inlet thermodynamic conditions on solid fuel ramjet performances," *International Journal of Aerospace Engineering*, vol. 2021, Article ID 8868288, 2021.

[27] T. Derbidge and C. Powars, "Acceleration effects on internal insulation erosion," *29th Joint Propulsion Conference and Exhibit*, 1993, p. 1858, 1993.

[28] J. Crump and A. Amy, "Flight amplified erosion of head end internal insulation," *American Journal of Veterinary Research*, vol. 25, no. 2, pp. 618–636, 2013.

[29] M. Rybalko, E. Loth, and D. Lankford, "A Lagrangian particle random walk model for hybrid RANS/LES turbulent flows," *Powder Technology*, vol. 221, pp. 105–113, 2012.

[30] S. A. Morsi and A. J. Alexander, "An investigation of particle trajectories in two-phase flow systems," *Journal of Fluid Mechanics*, vol. 55, no. 2, pp. 193–208, 1972.

[31] T. H. Shih, W. W. Liou, A. Shabir, and J. Zhu, "A new k -$\epsilon$ eddy viscosity model for high Reynolds number turbulent flows," *Computers Fluids*, vol. 24, no. 3, pp. 227–238, 1995.

[32] F. R. Menter, "Eddy viscosity transport equations and their relation to the k-$\varepsilon$ model," *Journal of Fluids Engineering*, vol. 119, no. 4, pp. 876–884, 1997.

[33] D. W. Netzer, "Modeling solid-fuel ramjet combustion," *Journal of Spacecraft and Rockets*, vol. 14, no. 12, pp. 762–766, 1977.

[34] B. F. Magnussen and B. H. Hjertager, "On mathematical modeling of turbulent combustion with special emphasis on soot formation and combustion," *Symposium (International) on Combustion*, vol. 16, no. 1, pp. 719–729, 1977.

[35] K. King, "Boron particle ignition in hot gas streams," *Combustion Science and Technology*, vol. 8, no. 5-6, pp. 255–273, 1973.

[36] K. King, "Boron ignition and combustion in air-augmented rocket afterburners," *Combustion Science and Technology*, vol. 5, no. 1, pp. 155–164, 1972.

[37] M. K. King, "Ignition and combustion of boron particles and clouds," *Journal of Spacecraft & Rockets*, vol. 19, no. 4, pp. 294–306, 1982.

[38] S. C. Li and F. A. Williams, "Ignition and combustion of boron in wet and dry atmospheres," *Symposium on Combustion*, vol. 23, no. 1, pp. 1147–1154, 1991.

[39] P. J. Coelho, N. Duic, C. Lemos, and M. G. Carvalho, "Modelage de la chambre de combustion d'un statoreacteur a combustible solide avec reseaux multiblocs," *Aerospace Science and Technology*, vol. 2, no. 2, pp. 107–119, 1998.

[40] J. Hu, *Research on the Secondary Combustion Chamber Operation Process of Boron-Based Propellant Ducted Rockets*, National University of Defense Technology, 2006.

[41] V. M. Gremyachkin, A. G. Istratov, and O. I. Leipunskii, "Theory of combustion of a boron particle in oxygen in high-temperature environment," *Combustion, Explosion and Shock Waves*, vol. 15, no. 6, pp. 691–698, 1979.

[42] P. Kuang-Zhi, W. Ying-Hong, C. Chao, and C. Xiao-Long, "Measurement of combustion heat of boron," *Journal of Astronautics*, vol. 5, no. 1, pp. 1589–1592, 2008.

[43] J. Wang, B. Zha, W. Zhang, Y. Zhang, and Q. Su, "A new method for studying the ablation/erosion properties of silicone rubber composites based on multi-phase flow," *Journal of Rubber Research*, vol. 22, no. 2, pp. 59–68, 2019.

[44] G. Kurth, C. Bauer, T. Meyer, J. Ramsel, and A. Thumann, "Development and testing of a C/SiC combustion chamber for high speed throttleable ducted rocket applications," in *51st AIAA/SAE/ASEE Joint Propulsion Conference*, p. 4232, Orlando, FL, 2015.

[45] H. A. Bethe and M. C. Adams, "A theory for the ablation of glassy materials," *Journal of the aerospace sciences*, vol. 26, no. 6, pp. 321–328, 1959.

[46] M. C. Adams, "Recent advances in ablation," *ARS Journal*, vol. 29, no. 9, pp. 625–632, 1959.

[47] P. Thakre and V. Yang, "Mitigation of graphite nozzle erosion by boundary-layer control in solid propellant rocket motors," *Journal of Propulsion and Power*, vol. 25, no. 5, pp. 1079–1085, 2009.